Nanoscale

PAPER

View Article Online
View Journal | View Issue

Cite this: *Nanoscale*, 2023, **15**, 19671

Strong non-linear optical response of Sb_2Se_3 nanorods in a liquid suspension based on spatial self-phase modulation and their all-optical photonic device applications†

Nabanita Sen,[a] Nabamita Chakraborty,[a] Biswajit Das[a] and Kalyan Kumar Chattopadhyay *[a,b]

Received 14th September 2023,
Accepted 13th November 2023

DOI: 10.1039/d3nr04623k

rsc.li/nanoscale

The field of nonlinear optics is constantly expanding and gaining new impetus through the discovery of fresh nonlinear materials. Herein, for the first time, we have performed spatial self-phase modulation (SSPM) experiments with an emerging anisotropic Sb_2Se_3 layered material in a liquid suspension for an all-optical diode and all-optical switching application. The third-order broadband nonlinear optical susceptibility ($\chi^{(3)}_{singlelayer} \sim 10^{-9}$ esu) and nonlinear refractive index ($n_2 \sim 10^{-6}$ cm^2 W^{-1}) of Sb_2Se_3 have been determined using a 671 nm laser beam. This result could be unambiguously explained by the anisotropic hole mobility of Sb_2Se_3. The linear relationship of $\chi^{(3)}$ and carrier mobility emphasizes the establishment of nonlocal hole coherence, the origin of the diffraction pattern. Consequently, the time evolution of diffraction rings follows the 'Wind-Chime' model. A novel photonic diode based on Sb_2Se_3/SnS_2 has been demonstrated using the nonreciprocal propagation of light. The self-phase modulation (SPM) technique uses laser lights of different wavelengths and intensities to demonstrate the all-optical logic gates, particularly OR logic gates. The exploration of nonlinear optical phenomena in Sb_2Se_3 opens up a new realm for optical information processing and communication. We strongly believe that this result will help to underpin the area of optical nonlinearities among its various applications.

1. Introduction

The future of optical communication depends on the use of all-optical modulation technology.[1–3,4] Optical modulation refers to the alteration of an optical signal's phase, amplitude, and other parameters through physical means. This can be done either directly from the light source or through an external electric or optical field.[1,5–7] The strength of optical modulation is influenced by both the materials' nonlinear properties and the propagation path.[1,5–7] It is necessary to investigate the nonlinear properties of new quantum materials, specifically the nonlinear refractive index (n_2) and third-order nonlinear susceptibility $\chi^{(3)}$, to create photonic devices with the best possible functions.[1,5–7] Nonlinear optical responses are commonly investigated by different methods like the *Z*-scan method,[8,9] four-wave mixing,[10,11] spatial self-phase modulation (SSPM),[12,13] *etc*. SSPM, also known as the optical Kerr effect, is a nonlinear optical phenomenon where nonlocal and intraband carriers of the material oscillate at an optical frequency of 10^{14} Hz, forming diffraction ring patterns through self-focusing.[4] SSPM is a simple and straightforward technique compared to other methods requiring a complex experimental setup or data fitting.[12,13] This can create a diffraction ring pattern in the far field.[4,12,13] The SSPM diffraction ring pattern was first obtained in liquid crystals by Durbin *et al.*,[14,15] and the third-order nonlinear susceptibility of exfoliated graphene was determined by Wu *et al.*[16] by employing the SSPM method. Following this, there was a significant increase in research interest towards investigating the nonlinear properties of 2D layered materials using the SSPM technique due to its ability to facilitate strong light–matter interaction, effective bandgap modulation, and superior optoelectronic properties.[1,17–19] It is essential to note that the SSPM diffraction ring pattern originates from the external electric field associated with the strong laser beam, which is explained by electron coherence theory.[4,20–22] The origin of the SSPM diffraction ring pattern in 3D TaAs is attributed to laser induced

[a]*Thin Film and NanoScience Laboratory, Department of Physics, Jadavpur University, Kolkata, 700032, India. E-mail: kalyan_chattopadhyay@yahoo.com, kkc.juphy@gmail.com*
[b]*School of Materials Science & Nanotechnology, Jadavpur University, Kolkata-700032, India*

† Electronic supplementary information (ESI) available: Comparison table, graph of $\chi^{(3)}$–carrier mobility, formation and distortion of SSPM patterns. See DOI: https://doi.org/10.1039/d3nr04623k

hole coherence.[23] Significant progress has been achieved in SSPM experiments with various quantum materials, including different nanostructures such as nanowires, nanoparticles, colloidal nanocrystals, and 2D flakes. Scientists have also obtained nonlinear parameters during these observations.[24–26] Wu *et al.* demonstrated the first all-optical switching based on SSPM with two-color intraband coherence in gapped quantum materials.[4] The SSPM method has been successfully applied by various groups in diverse applications, such as energy conversion and photonic diodes.[27–31] There is a significant opportunity to discover SSPM effects in new quantum materials and utilize them in developing photonic devices for practical use.

Recently, low dimensional chalcogenide semiconducting materials, *e.g.*, MoS_2, $MoSe_2$, InSe, TaSe, Bi_2Te_3, *etc.*, have been mostly investigated through the SSPM method due to their ultrathin nature and advantageous electronic and optoelectronic properties.[1,27–31] The spatial self-phase modulation due to the intense laser beam results in the formation of multiple diffraction ring patterns in the far field for the liquid suspensions of these semiconducting materials. The nonlinear refractive index and third-order nonlinear susceptibilities of these materials are determined by their strong electron coherence interaction with the laser intensities. Sb_2Se_3 is a promising semiconductor for optoelectronics or photonics due to its high absorption coefficient ($>10^5$ cm^{-1}) in the visible region and decent carrier mobilities ($\mu_e \sim 15$ and $\mu_h \sim 42$ cm^2 V^{-1} s^{-1}). Also, it has a narrow band gap ranging from 1 to 1.2 eV.[32] Importantly, Sb_2Se_3 possesses a simple binary composition with a single and stable orthorhombic phase in which $[Sb_4Se_6]n$ nanoribbons are linked through van der Waals interaction along the x (100) and y (010) axes. In addition, the strong covalent bond along the z (001) axis causes Sb_2Se_3 nanostructures to grow intrinsically in a one-dimensional manner. However, owing to the dissimilar binding strength along the x, y and z axes ($z \gg x > y$), Sb_2Se_3 exhibits strong physical anisotropy, and its structure could be manipulated from bulk to either 1D or 2D by altering the physical conditions.[32–34] Concurrently, it exhibits strong optical anisotropy and polarization sensitivity. Owing to the multifunctional properties, Sb_2Se_3 nanostructures offer enormous applications in diverse areas, *e.g.*, photovoltaics,[35] photodetectors,[36] photoelectrochemical (PEC) water splitting,[37] thermoelectric devices,[38] *etc.* The potential use of the nonlinear optical properties of Sb_2Se_3 in all-optical modulation technology has not been fully investigated.

Here, we have identified Sb_2Se_3 as a promising candidate for investigating the nonlinear optical properties through the strong light–matter interaction, followed by a successful demonstration in all-optical device applications. For the first time, we have performed SSPM experiments with 1D Sb_2Se_3 nanorods to study their nonlinear optical properties and simultaneously implement them in all-optical device applications. After the interaction of the 671, 532, and 407 nm continuous laser beams with the Sb_2Se_3 nanorod suspension, concentric diffraction ring patterns are observed in the far field on the screen. With the help of the 'Wind-Chime' model, we explain the formation and deformation process of the diffraction rings formed during this SSPM experiment. Additionally, SnS_2 nanosheets are utilized for their reverse saturable absorption properties in showcasing an optical diode alongside Sb_2Se_3. The laser beam undergoes propagational symmetry-breaking when combined with Sb_2Se_3 and SnS_2 (Sb_2Se_3/SnS_2 → forward, and SnS_2/Sb_2Se_3 → reverse direction), resulting in non-reciprocal propagation of light and the formation of an all-optical diode. We have successfully demonstrated an all-optical logic function, specifically the OR logic gate, using Sb_2Se_3 by manipulating the SPM of two lasers with 671 and 532 nm wavelengths.

2. Results and discussion

The XRD patterns in Fig. 1(a) demonstrate highly polycrystalline Sb_2Se_3, corresponding to the orthorhombic phase with the space group *Pbnm* (62) (JCPDS card no. 15-0861). The Raman spectrum in Fig. 1(b) shows prominent peaks at 115, 187, 251, 369 and 446 cm^{-1} which indicate the formation of phase-pure Sb_2Se_3.[33] The peak at 115 cm^{-1} is ascribed to the Se–Se bond vibration and the peak at 187 cm^{-1} is ascribed to the Sb–Se heteropolar stretching vibrational mode in the $Sb_2Se_{3/2}$ pyramids.[33] The Sb–Sb bond vibration in the (Se_2Sb–$SbSe_2$) structural unit arises at 251 cm^{-1}, whereas Sb–Se stretching vibrations originate at 369 and 446 cm^{-1}.[33] The FESEM micrograph (Fig. 1c) shows Sb_2Se_3 NRs with diameter <1 μm and length <10 μm. Also, the surface morphology is probed by

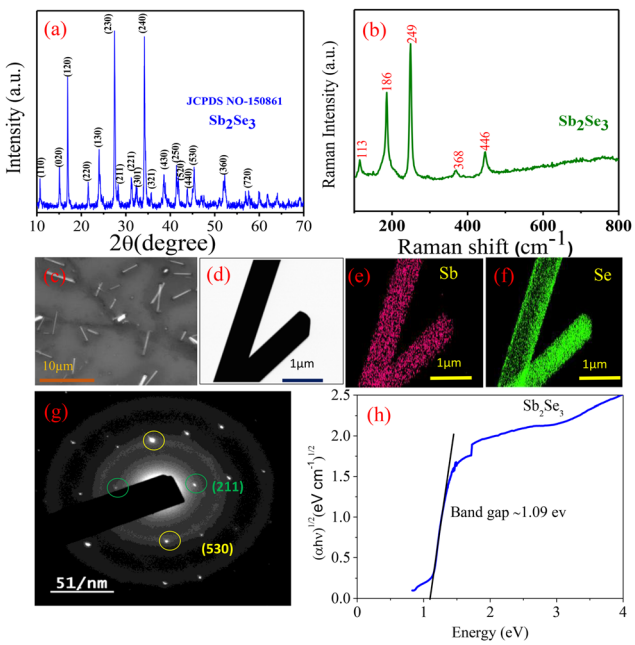

Fig. 1 Characterization studies of Sb_2Se_3 NRs: (a) XRD pattern, (b) Raman spectra, (c) scanning electron microscopy image, (d) transmission electron microscopy image, (e and f) FETEM colour mapping of Sb and Se, (g) selected area electron diffraction pattern and (h) Kubelka–Munk plot.

TEM (Fig. 1d) which corroborates well with the FESEM image. Furthermore, FETEM micrographs in Fig. 1(e and f) suggest that Sb and Se elements are uniformly distributed throughout the nanorods. Fig. 1(g) presents the selected area electron diffraction pattern, corroborating the presence of the (211) and (530) planes in alignment with the XRD pattern of the Sb_2Se_3 nanorods. Moreover, Sb_2Se_3 possesses an indirect bandgap of ~1.09 eV as obtained by the Kubelka–Munk plot shown in Fig. 1(h) and is therefore sensitive to electronic excitation of laser beams employed for our investigation.

2.1 The SSPM effect dominated by the nonlinear Kerr effect: nonlinear refractive index

Fig. 2(a) displays a brief schematic of our experimental setup, where a coherent and continuous laser with different wavelengths (45, 532, and 671 nm) has been focused onto the suspended solution of Sb_2Se_3 by a lens with a focal length of 200 mm. Focused laser light illuminates the suspended Sb_2Se_3 solution inside a quartz cuvette, and the strong nonlinearity of the material induces a self-focusing effect and forms a concentric diffraction ring in the far field. These diffraction rings appear due to the optical Kerr effect, wherein a phase shift of the coherent laser beam has been observed during the propagation through the Sb_2Se_3 suspension. Due to the thermal effect, these concentric diffraction rings are distorted and vertically deformed and become stable after some time. A digital camera has been placed behind the white screen to capture the continuous variation in the formation, deformation, and steady state of these diffraction rings. According to the optical Kerr effect, the refractive index (n) of the materials has a strong dependence on the intensity (I) of the incident laser light and the relation between them has been presented as $n = n_0 + n_2I$, where n_0 and n_2 are the linear and nonlinear refractive index of the material, respectively.[39] The phase shift ($\Delta\psi(r)$) of the incident Gaussian laser beam ($\psi(r)$) has strong dependence upon the n_2 of the material in the SSPM experiment, and it can be expressed as[40]

$$\Delta\psi(r) = \frac{2\pi n_0}{\lambda}\int_0^{L_{\text{eff}}} n_2 I(r,z)\mathrm{d}z \quad (1)$$

where $r\in[0, \infty)$ is the radial co-ordinate, λ is the wavelength of the incident laser beam and L_{eff} is the effective propagation path passing through the Sb_2Se_3 dispersion. For a Gaussian light beam, the central light intensity (I (0, z)) is twice the value of average light intensity (I). This phase modulation of the output beam is proportional to the incident intensity

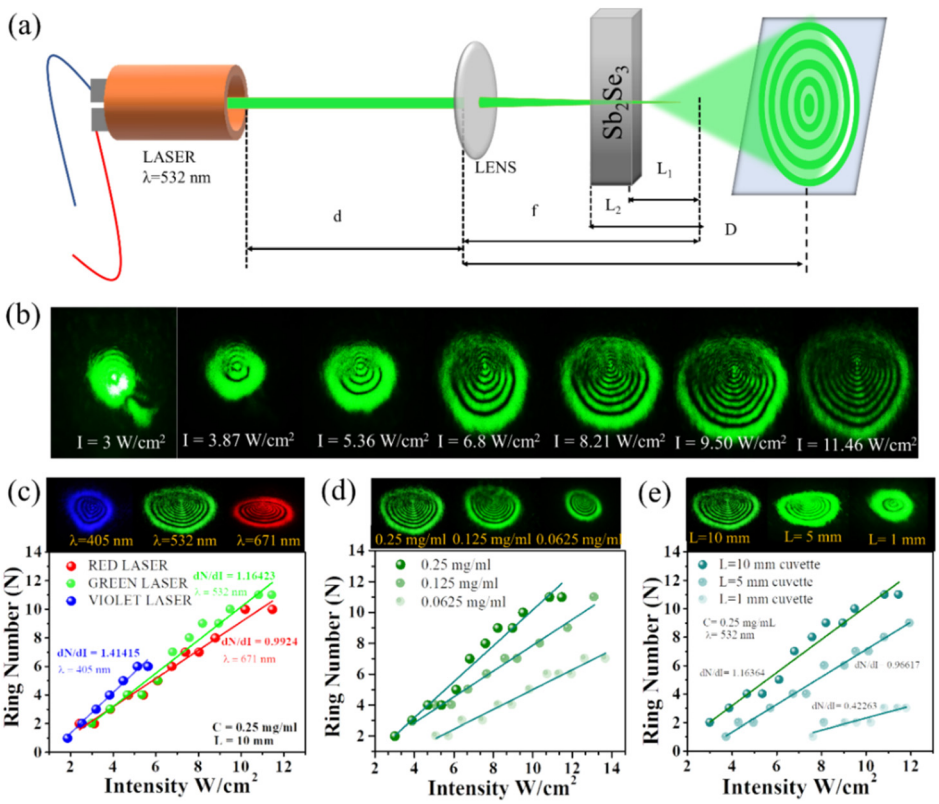

Fig. 2 Schematic of the SSPM experiment under various conditions: (a) schematic diagram of the experimental setup of spatial self-phase modulation (SSPM), (b) the real image of SSPM phenomena of a 532 nm laser beam, (c) SSPM ring number variation with intensity at the excitation of continuous laser beams of wavelength λ = 671, 532, and 405 nm, (d) the variation of diffraction ring numbers with incident laser (λ = 671 nm) intensity with cuvette lengths of 1, 5 and 10 mm, and (e) the diffraction ring number *vs.* the intensity of the laser (λ = 671 nm) with various concentrations of Sb_2Se_3 (0.25 mg ml^{-1}, 0.0625 mg ml^{-1}, and 0.03125 mg ml^{-1}).

($I(r, z)$) of the laser beam. The diffraction ring number (N) can be expressed as[16]

$$\Delta\psi(r_1) - \Delta\psi(r_2) = 2M\pi \quad (2)$$

where M is the integer number, and an odd or even value of M corresponds to the dark or bright diffraction pattern, respectively. From the following equation, L_{eff} of the laser beam can be determined:[41,42]

$$L_{\text{eff}} = \int_{L_1}^{L_2} \left(1 + \frac{z^2}{z_0^2}\right)^{-1} \mathrm{d}z = z_0 \tan^{-1}\left[\frac{z}{z_0}\right]_{L_1}^{L_2} \quad (3)$$

where $z_0 = \pi\omega_0^2/\lambda$, with $\omega_0 = 1/e^2$ being the beam radius; L_1, L_2 are the distances from the focus (f) to the side of the quartz cuvette; and z_0 is the diffraction length. Therefore, the nonlinear refractive index of Sb_2Se_3 can be determined from the formula[31]

$$n_2 = \frac{\lambda}{2n_0 L_{\text{eff}}} \frac{\mathrm{d}N}{\mathrm{d}I} \quad (4)$$

Subsequently, the third order nonlinear susceptibility $\chi^{(3)}_{\text{total}}$ of Sb_2Se_3 can be determined by[29,31]

$$\chi^{(3)}_{\text{total}} = \frac{cn_0^2}{12\pi^2} 10^{-7} n_2 \,(\text{esu}) \quad (5)$$

where c is the velocity of light in free space. As Sb_2Se_3 is a layered material, the nonlinear susceptibility of a single layer has a significant role and can be determined by[29,31]

$$\chi^{(3)}_{\text{total}} = \chi^{(3)}_{\text{singlelayer}} \times N_{\text{eff}}^2 \quad (6)$$

Here N_{eff} is the effective number of charge carrier layers present in the material and the calculation of the effective number of charge carrier layers is given in the ESI†.

Fig. 2(b) shows the variation of the diffraction ring numbers as a function of the intensity of the incident laser beam (532 nm). Each picture presented is taken after a sufficient duration of laser exposure on the sample, and the corresponding images present their steady condition. The results show that the number of rings and their diameter increase with the increase of the laser beam intensity, which arises due to the strong nonlinear response of Sb_2Se_3. To quantify this nonlinear response, the experimental results for all wavelengths (405, 532, and 671 nm) are also presented in Fig. 2(c). The solid points represent our experimental data, and the straight line is fitted linearly based on the experimental data. The corresponding slopes ($\mathrm{d}N/\mathrm{d}I$) are 0.9924, 1.1642, and 1.4142 for wavelength λ = 671, 532, and 407 nm, respectively. The upper panel of Fig. 2(c) displays the respective diffraction images at the highest intensity for all three incident laser lights. The nonlinear refractive index ($n_2 = 7.12 \times 10^{-6}$ cm^2 W^{-1}) and third-order nonlinear susceptibility ($\chi^{(3)} = 0.00343$ esu) have been determined using eqn (4) and 5) for λ = 532 nm. The n_2 and $\chi^{(3)}$ for other wavelengths are also calculated and presented in Table 1. Therefore, it is evidenced that the slope increases as the wavelength decreases, conclusively showing that a higher photon energy produces higher SSPM effects which corroborate well with previous investigations of different semiconducting materials, and a comparison has been presented in the ESI.† [1,27]

The diffraction patterns are formed due to SSPM, which depends on the active materials' concentration and the laser beam's effective path length.[31] To observe the above dependency, we further validate the SSPM experiments with different concentrations (C: 0.25, 0.125, and 0.0625 mg ml^{-1}) of the active Sb_2Se_3 NR suspension in a fixed length cuvette (L = 10 mm) and also for various cuvette thicknesses (L: 10, 5, 1 mm) with a fixed concentration of Sb_2Se_3 NRs (0.25 mg ml^{-1}). The above experiment was performed with a λ = 532 nm laser, and the corresponding results are presented in Fig. 2(d) and (e), respectively. The corresponding stable diffraction patterns at the maximum intensity are presented in the top panel of Fig. 2(d) and (e). The calculated nonlinear refractive index (n_2) and third-order nonlinear susceptibility $\chi^{(3)}$, along with the concentration of the active material and cuvette thickness variations, are listed in Table 1. The results indicate that the effective path length plays a crucial role in diffraction ring formation. As the effective path length increases, either by increasing the dispersion concentration or by increasing the cuvette thickness, the slopes $\mathrm{d}N/\mathrm{d}I$ also increase (see Table 1), which necessarily alters the nonlinear properties of the active Sb_2Se_3 NR dispersion. Again, N_{eff} also depends on the number of molecules present in the cuvette, *i.e.* the concentration. A lower concentration along with a narrower cuvette width results in fewer layers in the cuvette, and the reduced N_{eff} leads to a higher $\chi^{(3)}_{\text{singlelayer}}$, which are listed in Table 1.

2.2 Wind-Chime model

By manipulation of laser light, Sb_2Se_3 NRs in a homogeneous NMP solution form diffraction rings, the origin of which is

Table 1 Variation of nonlinear refractive index and third-order nonlinear susceptibility with various parameters

Experimental condition	λ (nm)	L (mm)	C (mg ml^{-1})	$\frac{\mathrm{d}N}{\mathrm{d}I}$ (cm^2 W^{-1})	n_2 ($\times 10^{-6}$ cm^2 W^{-1})	$\chi^{(3)}_{\text{total}}$ [esu]	$\chi^{(3)}_{\text{singlelayer}}$ [$\times 10^{-9}$ esu]
Wavelength variation	671	10	0.25	0.9924	6.67	0.00423	1.05
	532	10	0.25	1.16423	7.12	0.00343	0.85
	405	10	0.25	1.41415	9.12	0.00228	0.57
Concentration variation	532	10	0.2500	1.16423	7.12	0.00343	0.85
	532	10	0.1250	0.8372	7.05	0.00179	1.55
	532	10	0.0625	0.641	5.39	0.00137	4.73
Cuvette thickness variation	532	10	0.25	1.16423	7.12	0.00343	0.85
	532	5	0.25	0.96617	16.2	0.00414	3.58
	532	1	0.25	0.42263	35.6	0.00907	198

successfully described by the 'Wind-Chime' model.[4] The applicability of 'Wind-Chime' model involves carrier coherence (electrons or holes) and ring formation time. Here when an optical electromagnetic wave (10^{14} Hz) is incident on atomic charged particles (such as electrons and holes), they undergo forced oscillation and respond by re-radiating the wave with the same frequency. Quasiparticles which are subjected to forced oscillation are coherent to the incoming E.M. wave and they are mutually coherent with one another. The strength of re-radiation depends on how easily charged particles move back and forth with the incoming wave. The main limitation of the back-and-forth oscillations is the tendency of the material's electronic distribution to revert to its preferred electronic state. Nonetheless there is a balance between the effect of the incident E.M. wave causing movement of the carriers and the restoring force which tries to regain the equilibrium. This behaviour is quantitatively described by the mobility of the charged particles. Sb_2Se_3 is a p type material and its $\chi^{(3)}$ has a good degree of co-relation with its hole mobility ($\mu_h \sim 42\ cm^2\ V^{-1}\ s^{-1}\mu_e \sim 15$)[29] [ESI Fig. S1†]. Moreover, it fits well with an empirical relation which emphasizes the dominance of hole coherence in the formation of diffraction ring patterns. As hole mobility is not much greater than electron mobility in Sb_2Se_3, the electronic contribution to the origin of coherence is inevitable. In-plane carrier mobilities are profoundly dominated in 2D materials. Sb_2Se_3 possesses anisotropic carrier mobility due to its van der Waals bond along the x and y axes and covalent bond along the z axis. However, because of distinctive carrier mobilities along different directions it exhibits torque. Hence the alignment of Sb_2Se_3 NRs takes some time to form ring patterns. The dielectric environment and refractive index contribute to the time required for ring formation. Fig. 3(a) presents a schematic illustration of the 'Wind-Chime model'. According to the 'Wind-Chime' model, the time required to attain the maximum diameter of the ring is the time required to fully align all the Sb_2Se_3 NRs with the field direction. This phenomenon has been experimentally observed for all three laser sources (671, 532, and 405 nm) and the snapshots at different times during the dynamic ring formation process are presented in Fig. 3(b–d). The evolution time of ring formation follows the exponential model as below:[4,42]

$$N = A\left(1 - e^{-\frac{t}{t_c}}\right) \tag{7}$$

where N is the number of rings, t_c is the rising time for ring formation and A is a constant. Fig. 3(e) shows the ring number

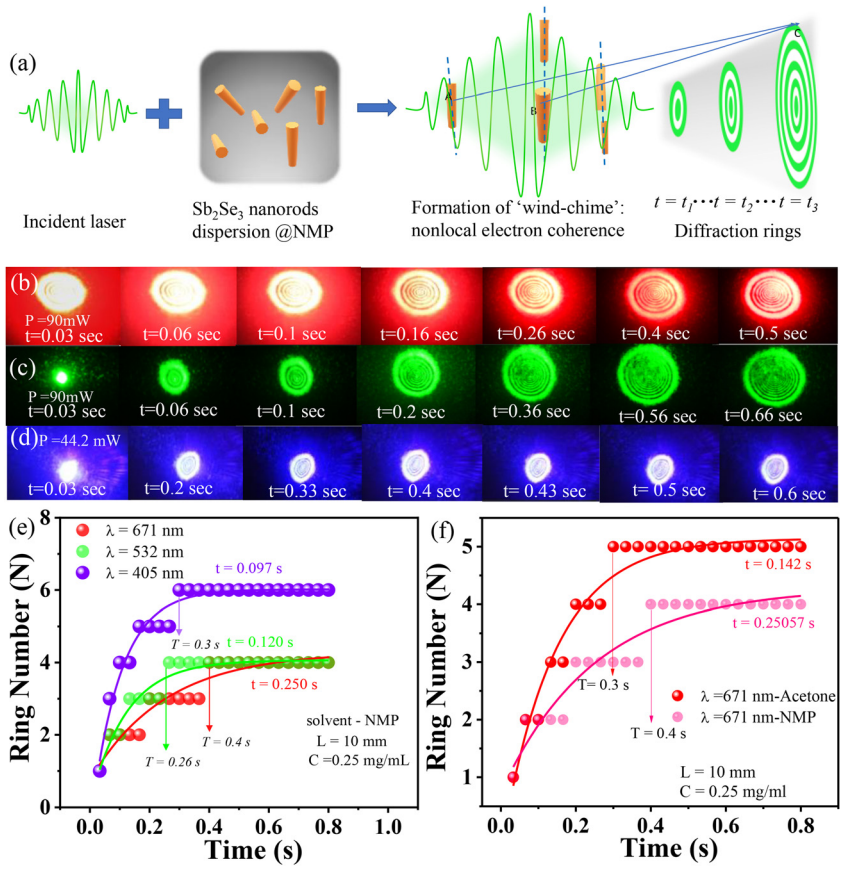

Fig. 3 Experimental verification of the 'Wind-Chime' model: (a) schematic illustration of the 'Wind-Chime' model showing the mechanism of light–matter interaction and related diffraction pattern. (b–d) Diffraction ring pattern appeared on the screen as a function of time for wavelengths 671, 532 and 405 nm respectively. Time evolution of diffraction rings: (e) diffraction ring numbers *vs.* time at intensities I = 5.36, 5.36, and 5.62 W cm^{-2} for wavelengths 671, 532 and 405 nm and (f) the effect of different viscous media (NMP and acetone) for a wavelength of 671 nm.

vs. time graph which is fitted with the above function. The rising times of diffraction patterns for the λ = 671, 532, and 405 nm lights are estimated to be 0.25, 0.12, and 0.09 s, respectively. Also, from the 'Wind-Chime' model, the time required for aligning most of the nanodomains inside the viscous medium can be presented as $T = \frac{\varepsilon\pi\eta\xi RC}{1.72(\varepsilon-1)Ih}$ where ε is the relative dielectric constant of Sb_2Se_3, η is the coefficient of viscosity of the solvent, R is the Sb_2Se_3 domain radius, h is the thickness of Sb_2Se_3, and I is the laser intensity. The minimum time required to reach the highest number of rings for wavelengths 671, 532, and 405 nm has been experimentally determined to be T = 0.4, 0.26 and 0.3 s, respectively. Here, the intensities considered for the ring formation are I = 5.36, 5.36 and 5.62 W cm^{-2} for λ = 671, 532, and 405 nm, respectively. In addition, T also depends on the viscosity of the solvent and the related experimental results are provided in Fig. 3(f). The values of τ in solvents NMP (η = 1.65 × 10^{-3} Pa s) and acetone (η = 3.2 × 10^{-4} Pa s) are 0.4 and 0.3 s respectively for a wavelength of 671 nm. According to the 'Wind-Chime' model, time T is proportional to the viscosity of the solvent. Hence the experimental results validate the 'Wind-Chime' model.

2.3 Dynamics of the deformation phenomena of the SSPM diffracted laser beam

The diffraction patterns are spread into perfect concentric rings which attain maximum diameter through the 'Wind-Chime' alignment of the Sb_2Se_3 NRs owing to interaction with

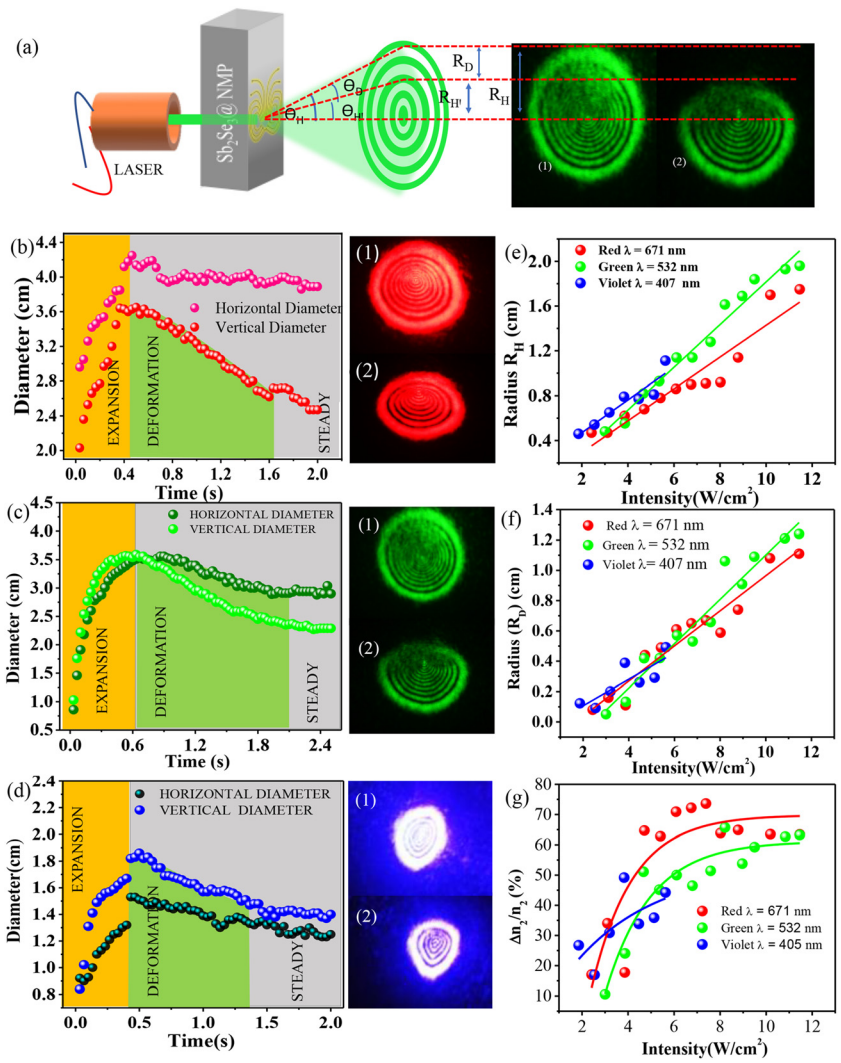

Fig. 4 Evolution of diffraction rings in SSPM: (a) schematic illustration of the deformation phenomenon of diffraction rings. (b)–(d) Horizontal and vertical ring diameter evolution over time and their corresponding real SSPM patterns at maximum and distorted conditions for wavelengths 671, 532, and 405 nm respectively. (e) Maximum radius (R_H) *versus* incident laser intensity at the maximum ring evolution condition and (f) distorted radius (R_D) *versus* incident laser intensity at the distorted ring condition for different laser beam wavelengths of 671, 532, and 405 nm. (g) Relative change in the nonlinear refractive index with incident laser light intensity for wavelengths 671, 532 and 405 nm.

the laser's electric field. Due to the thermal effect, especially vertical thermal convection, a concentration gradient of Sb_2Se_3 has been established along the optical path.[39] Therefore, the vertical upper half of the diffraction patterns is distorted compared to the lower half. Fig. 4(a) shows the schematic and experimental results of the distortion. This deformation process is due to thermal convection, and it must depend upon the energy of the photons and the intensity of the incident laser beam. The details on the formation and deformation process of diffraction rings can be found in ESI Fig. S2†. To verify the above statement, we have measured the dynamic change of the vertical and horizontal diameters for all the lasers at their highest intensities. Fig. 4(b)–(d) present the change in diameter under the expansion, deformation and stable conditions for λ = 671, 532, and 405 nm, respectively. The side panel of the respective figures shows the maximum expansion and stable conditions. From the above data, the deformation times are obtained as 1, 1.534 and 0.9 s for 671 nm (I = 11 W cm^{-2}), 532 nm (I = 11 W cm^{-2}), and 405 nm (I = 5.5 W cm^{-2}), respectively. Also, this dynamic deformation process can be quantified by the half cone angle (θ_H) of the diffraction pattern formed by the laser beam (Fig. 4(a)) using the following expression:[43]

$$\theta_H = n_2 I\left[-\frac{8rL}{\omega_0^2}\exp\left(-\frac{2r^2}{\omega_0^2}\right)\right]_{max} \quad (8)$$

where $\left[-\frac{8rL}{\omega_0^2}\exp\left(-\frac{2r^2}{\omega_0^2}\right)\right]$ is a constant = K and $r\in[0, \infty)$. So, θ_H is proportional to the nonlinear refractive index. During the deformation process, due to thermal convection, the concentration gradient of Sb_2Se_3 NRs changes between the upper and lower halves of the optical path, which breaks the diffraction patterns' axial symmetry. As a result, the nonlinear refractive index has also been changed from n_2 to n'_2.

Therefore, the relative change in the nonlinear refractive index has been expressed by the deformation angle θ_D as

$$\theta_D = (\theta_H - \theta_{H'}) = (n_2 - n'_2)IK = \Delta n_2 IK \quad (9)$$

Using the above expressions, θ_D/θ_H can be expressed as $\Delta n_2/n_2$.

Using simple trigonometry, the half angles are converted into the radius of the diffraction rings, and the relative change

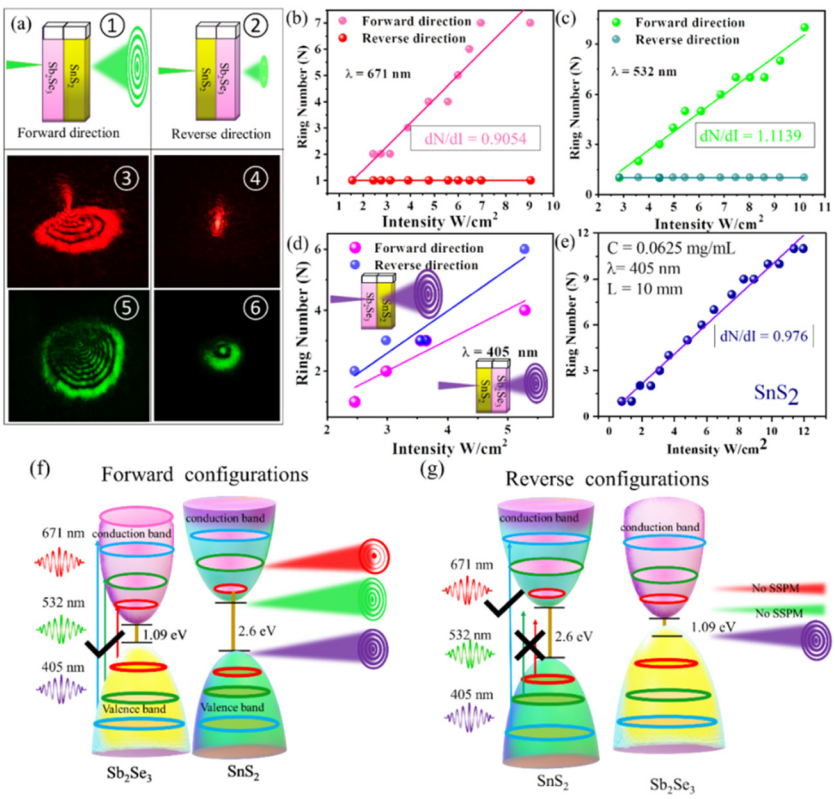

Fig. 5 All-optical diode application: (a) (1–2) schematic presentation of nonreciprocal light propagation in forward and reverse directions. (3–4) Diffraction patterns obtained for 671 nm wavelength under forward and reverse conditions respectively. (5–6) Diffraction patterns obtained for 532 nm wavelength in forward and reverse conditions respectively. The experimental results obtained for a nonlinear photonic diode with the hybrid structure Sb_2Se_3/SnS_2 for incident laser lights of wavelengths (b) 671 nm and (c) 532 nm. (d) Experimentally obtained intensity *vs.* diffraction ring number for the photonic diode Sb_2Se_3/SnS_2 for a wavelength of 405 nm. (e) Intensity *vs.* diffraction ring number for SnS_2 for a wavelength of 405 nm. Schematic presentation of the band diagram model for (f) the forward configuration of Sb_2Se_3/SnS_2 and (g) the reverse configuration of Sb_2Se_3/SnS_2.

in the nonlinear refractive index can be expressed as $\frac{\Delta n_2}{n_2} = \frac{\Delta\theta_D}{\theta_H} = \frac{R_D}{R_H} = \frac{R_H - R_{H'}}{R_H}$.[44,45] Fig. 4(e and f) present the experimentally measured maximum vertical radius (R_H) before the deformation process and the radius after the deformation (R_D) as a function of the intensity of the incident laser for all the wavelengths. Moreover, Fig. 4(g) depicts the relative change in the nonlinear refractive index $\Delta n_2/n_2$ of Sb_2Se_3 NRs with the intensity of the incident laser, which has been determined to be 69% (for 11 mW cm^{-2}), 60% (for 11 mW cm^{-2}) and 42% (for 5.55 mW cm^{-2}) for red (671 nm), green (532 nm) and violet (432 nm) lasers, respectively.

2.4 Demonstration of an all-optical diode ($Sb_2Se_3 \leftrightarrow SnS_2$)

Sb_2Se_3 NRs exhibit a strong optical Kerr effect and show a high nonlinear refractive index and third-order nonlinear susceptibility as compared to other chalcogenide-based 2D materials. This nonlinear property has been used to construct an Sb_2Se_3 NRs/SnS_2 hybrid structure for an all-optical diode application. Initially, Sb_2Se_3 NRs and SnS_2 with the same concentration were dispersed in an NMP solution and put in two different cuvettes placed side-by-side to construct an all-optical diode. These two cuvettes were placed in front of the optical path of the coherent laser light. Laser light was passed through two configurations. One is through Sb_2Se_3 first and then through SnS_2, and the other configuration is through SnS_2 first and then through Sb_2Se_3. Compared to the electronic diode structure, the first one is called a forward configuration, and the latter is called a reversed configuration. Both configurations have been schematically presented in Fig. 5(a) ① and ②, respectively. As the name suggested, in the forward configuration, the SSPM phenomena occurred, and the diffraction rings are observed on the screen for the lasers of wavelengths 671 and 532 nm (Fig. 5(a) ③, ⑤). Similarly, no SSPM happened in the reverse configuration, and no diffraction rings are observed in the far field (Fig. 5(a) ④, ⑥). This all-optical diode for l = 671 and 532 nm is observed for the entire intensity range, and the results are presented in Fig. 5(b) and (c), respectively. This diode response was not observed for the 405 nm laser light. Both the forward and reverse configurations showed SSPM, and the diffraction ring variation with intensity is presented in Fig. 5(d). The above effect is attributed to the reverse saturation absorption property of SnS_2.[31] The bandgap of SnS_2 is 2.6 eV, which is larger than the forbidden bandgap range corresponding to the wavelengths 671 and 532 nm. However, a 405 nm laser can create SSPM in SnS_2; the results are presented in Fig. 5(e). Hence, 671 and 532 nm lasers do not induce any interaction with SnS_2, and as a result, in the reverse configuration, all lights are absorbed by SnS_2, and the remaining light does not have enough intensity to interact with Sb_2Se_3 to create SSPM. From the band diagram model, we schematically present both forward and reverse configurations in Fig. 5(f) and (g), respectively.

3.5 Sb_2Se_3 optical modulator/switcher based on SSPM

Taking advantage of the strong optical Kerr effect, Sb_2Se_3 NRs can be used not only in an all-optical diode but also for all-optical logic functions like an OR gate using the self-phase modulation (SPM) technique. Here, a relatively strong laser light has been employed to modulate the propagation of another laser light with relatively weak intensity. The experimental setup for this light–light modulation technique has been schematically presented in Fig. 6(a). Here, the SPM technique has been employed for two laser sources i.e. 671 and 532 nm and they are allowed to interact through the Sb_2Se_3 NRs. The low and high intensities of the lasers are designated as "0" and "1" states in the input, and the diffraction ring due to SPM (when both the lasers show diffraction rings) has to be considered "1"; otherwise, the output is "0". Fig. 6(b) shows the symbolic and wavefront presentation of the OR logic gate. Two inputs, "A" and "B", are considered corresponding to 671 and 532 nm lasers, respectively. When both the lasers have low intensity, they cannot create any diffraction ring pattern on the screen, so for "0", "0" input, we get "0" output. Again, when both the lasers are at the highest intensities, they create diffraction rings on the screen. This state can be designated as "1", "1" input, and we obtain "1" as the output. But interestingly, when any one has low power and the others have high power, we also get the diffraction rings for both lasers in the output. This happens due to the SPM of

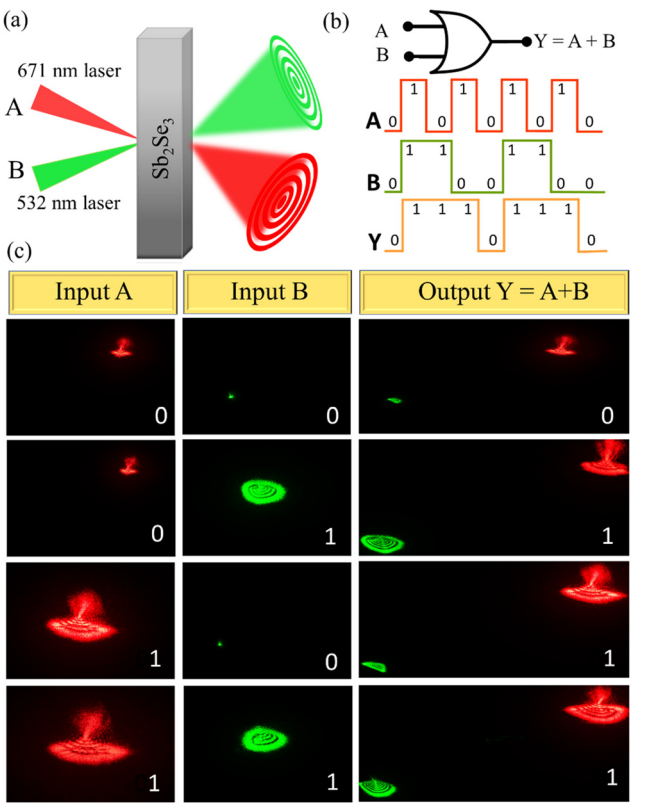

Fig. 6 All-optical logic application: realization of all-optical modulation by self-phase modulation and demonstration of the OR logic function. (a) Schematic of the light–light modulation system, (b) two input OR gate: input and output waveform of the OR logic operation and (c) experimental results of the OR logic operation with 671 and 532 nm laser beams.

lights passing through the Sb_2Se_3 NRs. As a result, the output is "1" whenever anyone's input is "1". This function is typically an OR logic function. The experimental results are presented in a truth table format in Fig. 6(c). In summary, these two laser lights can achieve mutual modulation using the strong optical Kerr effect of Sb_2Se_3 NRs.

3. Conclusion

In summary, after the measurement and calculation, we found that the Sb_2Se_3 NRs could serve as a narrow bandgap material, eliciting strong nonlinear optical responses, especially a high nonlinear refractive index (n_2) and third-order nonlinear susceptibility $\chi^{(3)}$, for the first time using the SSPM technique. The strong light–matter interaction between the intense laser light (λ = 671, 532, and 405 nm) and Sb_2Se_3 NRs results in diffraction ring patterns in the far field. These nonlinear properties strongly depend upon the wavelength of the laser, the concentration of NRs and the effective optical path lengths. The 'Wind-Chime' model was used to analyze the formation process of these diffraction rings, and the distortion of the diffraction rings was explained by the thermal convection through suspended NRs. By taking advantage of the strong optical Kerr effect and reverse saturation absorption properties of Sb_2Se_3 and SnS_2, we have demonstrated an all-optical diode for 671 and 532 nm laser sources. Furthermore, a novel, all-optical logic function, the OR logic gate, has been demonstrated by taking advantage of SPM, where a weak light can be modulated in the presence of a strong light due to the strong nonlinear response of Sb_2Se_3 NRs. Therefore, exploring the nonlinear optical properties of Sb_2Se_3 NRs and demonstrating all-optical diode and logic applications could pave the way for developing future devices utilizing all-optical signal processing.

4. Experimental sections

4.1 Synthesis of Sb_2Se_3 nanorods

Sb_2Se_3 was synthesized by a typical solvothermal procedure.[33] First, 0.086 g of $SbCl_3$ was dissolved in 75.8 ml of DEG and then ammonia was added under magnetic stirring. Afterward, sodium sulphite (0.095 g) and Se powder (0.048 g) were mixed into the solution under continuous stirring. Then the as-prepared mixture was transferred into a 100 ml Teflon-lined stainless-steel autoclave and heated for 22 hours at 180 °C. After completing the process, the mixture was cooled down normally and the products were filtered by the vacuum filtration method. Then, the sample was consecutively washed with deionized water and absolute ethanol. Finally, the sample was dried in a vacuum oven at 80 °C overnight for further use.

4.2 Synthesis of SnS_2 nanosheets

SnS_2 nanosheets were synthesized using the procedure previously reported by Zhang *et al.*[46] In a typical procedure, $SnCl_4{\cdot}5H_2O$ (220 mg) and thioacetamide (280 mg) were added in 60 mL of DI water and stirred unless mixed. After that, the solution was transferred into a 100 mL Teflon-lined autoclave for heating at 180 °C for 24 h. Then the autoclave was naturally cooled down to room temperature before collecting the yellow colored samples by a centrifugation process (10 000 rpm). After collecting, the samples were dried in a hot air oven at 80 °C for 6 h and stored carefully before further utilization.

4.3 Material characterization

The crystallinity of Sb_2Se_3 was determined using X-ray diffraction at room temperature with a Rigaku Ultima III X-ray diffractometer using Cu Kα radiation with a wavelength of 1.54 Å. Raman spectroscopy (Witech) was employed to obtain the characteristic vibrational mode of Sb_2Se_3. Surface morphology was revealed by field emission scanning electron microscopy (FESEM, Hitachi, S-4800) and high-resolution transmission electron microscopy (HRTEM, JEOLJEM 2100). TEM-EDX (transmission electron microscopy-energy dispersive X-ray spectroscopy) elemental mapping shows the chemical composition and stoichiometric ratio of Sb_2Se_3. The bandgap was determined using the Kubelka–Munk plot derived from UV-visible diffuse reflectance spectroscopy.

Conflicts of interest

There are no conflicts to declare.

Acknowledgements

The authors would like to thank the University Grants Commission (UGC), Government of India, for the UPE II scheme. The author NS acknowledges the University Grants Commission (UGC), for awarding her a Senior Research Fellowship (SRF), Government of India [File No: 16-9(June 2018)/2019(NET/CSIR)]. BD acknowledges the Council of Scientific and Industrial Research (CSIR-RA) (File No. 09/028 (1096)/2019-EMR-I) programme. NC wishes to thank the Department of Science and Technology (DST), Government of India, for awarding her a DST-INSPIRE research fellowship (DST/INSPIRE Fellowship/IF200516).

References

1 L. Wu, X. Yuan, D. Ma, Y. Zhang, W. Huang, Y. Ge, Y. Song, Y. Xiang, J. Li and H. Zhang, *Small*, 2020, **16**, 2002252.
2 D. Pacifici, H. J. Lezec and H. A. Atwater, *Nat. Photonics*, 2007, **1**, 402.
3 M. Hochberg, T. Baehr-Jones, G. Wang, M. Shearn, K. Harvard, J. Luo, B. Chen, Z. Shi, R. Lawson, P. Sullivan, A. K. Y. Jen, L. Dalton and A. Scherer, *Nat. Mater.*, 2006, **5**, 703.
4 Y. L. Wu, Q. Wu, F. Sun, C. Cheng, S. Meng and J. Zhao, *Proc. Natl. Acad. Sci. U. S. A.*, 2015, **112**, 11800.
5 E. Wong, K. L. Lee and T. B. Anderson, *J. Lightwave Technol.*, 2007, **25**, 67.

6 Q. Bao, H. Zhang, Y. Wang, Z. Ni, Y. Yan, Z. X. Shen, K. P. Loh and D. Y. Tang, *Adv. Funct. Mater.*, 2009, **19**, 3077.
7 Y. Wang, W. Huang, C. Wang, J. Guo, F. Zhang, Y. Song, Y. Ge, L. Wu, J. Liu, J. Li and H. Zhang, *Laser Photonics Rev.*, 2019, **13**, 1800313.
8 Y. Xu, W. Wang, Y. Ge, H. Guo, X. Zhang, S. Chen, Y. Deng, Z. Lu and H. Zhang, *Adv. Funct. Mater.*, 2017, **27**, 1702437.
9 Z. Guo, H. Zhang, S. Lu, Z. Wang, S. Tang, J. Shao, Z. Sun, H. Xie, H. Wang, X.-F. Yu and P. K. Chu, *Adv. Funct. Mater.*, 2015, **25**, 6996.
10 S. A. March, D. B. Riley, C. Clegg, D. Webber, X. Liu, M. Dobrowolska, J. K. Furdyna, I. G. Hill and K. C. Hall, *ACS Photonics*, 2017, **4**, 1515.
11 S. K. Turitsyn, A. E. Bednyakova, M. P. Fedoruk, S. B. Papernyi and W. R. L. Clements, *Nat. Photonics*, 2015, **9**, 608.
12 L. Lu, Z. Liang, L. Wu, Y. Chen, Y. Song, S. C. Dhanabalan, J. S. Ponraj, B. Dong, Y. Xiang, F. Xing, D. Fan and H. Zhang, *Laser Photonics Rev.*, 2018, **12**, 1700221.
13 L. Lu, X. Tang, R. Cao, L. Wu, Z. Li, G. Jing, B. Dong, S. Lu, Y. Li, Y. Xiang, J. Li, D. Fan and H. Zhang, *Adv. Opt. Mater.*, 2017, **5**, 1700301.
14 S. D. Durbin, S. M. Arakelian and Y. R. Shen, *Opt. Lett.*, 1981, **6**, 411.
15 S. D. Durbin, S. M. Arakelian and Y. R. Shen, *Phys. Rev. Lett.*, 1981, **47**, 1411.
16 R. Wu, Y. Zhang, S. Yan, F. Bian, W. Wang, X. Bai, X. Lu, J. Zhao and E. Wang, *Nano Lett.*, 2011, **11**, 5159.
17 S. Yu, X. Wu, Y. Wang, X. Guo and L. Tong, *Adv. Mater.*, 2017, **29**, 1606128.
18 Y. Gao, Y. Hu, C. Ling, G. Rui, J. He and B. Gu, *Nanoscale*, 2023, **15**, 6225.
19 J. E. Q. Bautista, C. L. A. V. Campos, M. L. da Silva-Neto, C. B. de Araujó, A. M. Jawaid, R. Busch, R. A. Vaia and A. S. L. Gomes, *ACS Photonics*, 2023, **10**, 484.
20 Y. L. Wu, L. L. Zhu, Q. Wu, F. Sun, J. K. Wei, Y. C. Tian, W. L. Wang, X. D. Bai, X. Zuo and J. Zhao, *Appl. Phys. Lett.*, 2016, **24**, 108.
21 W. Wang, Y. Wu, Q. Wu, J. Hua and J. Zhao, *Sci. Rep.*, 2016, **6**(1), 22072.
22 L. Hu, F. Sun, H. Zhao and J. Zhao, *Opt. Lett.*, 2019, **44**(21), 5214–5217.
23 Y. Huang, H. Zhao, Z. Li, L. Hu, Y. Wu, F. Sun, S. Meng and J. Zhao, *Adv. Mater.*, 2023, **35**(11), 2208362.
24 C. Wang, S. Xiao, X. Xiao, H. Zhu, L. Zhou, Y. Wang, X. Du, Y. Wang, Z. Yang, R. Duan, M. Zhong, H. Rubahn, G. Zhang, Y. Li and J. He, *J. Phys. Chem. C*, 2021, **125**(28), 15441.
25 R. Zamiri, A. Zakaria, M. B. Ahmad, A. R. Sadrolhosseini, K. Shameli, M. Darroudi and M. A. Mahdi, *Optik*, 2011, **122**, 836.
26 X. Wang, Y. Yan, H. Cheng, Y. Wang and J. Han, *Mater. Lett.*, 2018, **214**, 247.
27 Y. Liao, C. Song, Y. Xiang and X. Dai, *Ann. Phys.*, 2020, **532**, 2000322.
28 Y. Liao, Y. Shan, L. Wu, Y. Xiang and X. Dai, *Adv. Opt. Mater.*, 2020, **8**, 1901862.
29 Y. Shan, L. Wu, Y. Liao, J. Tang, X. Dai and Y. Xiang, *J. Mater. Chem. C*, 2019, **7**, 3811.
30 Y. Jia, Y. Liao, L. Wu, Y. Shan, X. Dai, H. Cai, Y. Xiang and D. Fan, *Nanoscale*, 2019, **11**, 4515.
31 K. Sk, B. Das, N. Chakraborty, M. Samanta, S. Bera, A. Bera, D. S. Roy, S. K. Pradhan, K. K. Chattopadhyay and M. Mondal, *Adv. Opt. Mater.*, 2022, **10**, 2200791.
32 K. Zeng, D. J. Xue and J. Tang, *Semicond. Sci. Technol.*, 2016, **31**, 063001.
33 N. Sen, A. Das, S. Maity, S. Ghosh, M. Samanta and K. K. Chattopadhyay, *ACS Appl. Energy Mater.*, 2023, **6**, 58.
34 H. Song, T. Li, J. Zhang, Y. Zhou, J. Luo, C. Chen, B. Yang, C. Ge, Y. Wu and J. Tang, *Adv. Mater.*, 2017, **29**, 1700441.
35 A. Mavlonov, T. Razykov, F. Raziq, J. Gana, J. Chantana, Y. Kawano, T. Nishimura, H. Weie, A. Zakutayev, T. Minemoto, X. Zua, S. Li and L. Qiao, *Sol. Energy*, 2020, **201**, 227.
36 T. Zhai, M. Ye, L. Li, X. Fang, M. Liao, Y. Li, Y. Koide, Y. Bando and D. Golberg, *Adv. Mater.*, 2010, **22**, 4530.
37 S. Chen, T. Liu, Z. Zheng, M. Ishaq, G. Liang, P. Fan, T. Chen and J. Tang, *J. Energy Chem.*, 2022, **67**, 508.
38 T. Y. Ko, M. Shellaiah and K. W. Sun, *Sci. Rep.*, 2016, **6**, 35086.
39 G. Wang, S. Zhang, F. A. Umran, X. Cheng, N. Dong, D. Coghlan, Y. Cheng, L. Zhang, W. J. Blau and J. Wang, *Appl. Phys. Lett.*, 2014, **104**, 141909.
40 Y. Jia, Y. Shan, L. Wu, X. Dai, D. Fan and Y. Xiang, *Photonics Res.*, 2018, **6**, 1040.
41 J. Zhang, X. Yu, W. Han, B. Lv, X. Li, S. Xiao, Y. Gao and J. He, *Opt. Lett.*, 2016, **41**, 1704.
42 S. Xiao, Y.-l. He, Y.-l. Dong, Y.-d. Wang, L. Zhou, X.-j. Zhang, Y.-w. Wang and J. He, *Front. Phys.*, 2021, **9**, 212.
43 G. Wang, S. Zhang, X. Zhang, L. Zhang, Y. Cheng, D. Fox, H. Zhang, J. N. Coleman, W. J. Blau and J. Wang, *Photonics Res.*, 2015, **3**, A51.
44 L. Wu, Z. Xie, L. Lu, J. Zhao, Y. Wang, X. Jiang, Y. Ge, F. Zhang, S. Lu, Z. Guo, J. Liu, Y. Xiang, S. Xu, J. Li, D. Fan and H. Zhang, *Adv. Opt. Mater.*, 2018, **6**, 1700985.
45 M. Zidan, M. El-Daher, M. Al-Ktaifani, A. Allahham and A. Ghanem, *Optik*, 2020, **219**, 165275.
46 J. Zhang, G. Huang, J. Zeng, Y. Shi, S. Lin, X. Chen, H. Wang, Z. Kong, J. Xi and Z. Ji, *J. Am. Ceram. Soc.*, 2019, **102**, 2810.